Pergamon

Acta mater. 49 (2001) 4149–4160

Acta MATERIALIA

www.elsevier.com/locate/actamat

CHARACTERIZATION OF THE MICROSTRUCTURE EVOLUTION IN A NICKEL BASE SUPERALLOY DURING CONTINUOUS COOLING CONDITIONS

S. S. BABU†, M. K. MILLER, J. M. VITEK and S. A. DAVID

Metals and Ceramics Division, Oak Ridge National Laboratory, Oak Ridge, TN 37831, USA

(Received 2 July 2001; received in revised form 30 July 2001; accepted 16 August 2001)

Abstract—The solidification characteristics of the γ phase from the liquid and the subsequent decomposition of the γ phase control the evolution of the microstructure in nickel–base superalloy welds. The precipitation of the γ' phase from the γ phase during continuous cooling conditions (0.17–75 K s^{-1}) from the solutionizing temperature was characterized in a directionally solidified CM247DS alloy with thermomechanical simulator, and by transmission electron microscopy, atom probe field ion microscopy and atom probe tomography. The number density increased; size decreased and morphology of the γ' precipitates changed with an increase in cooling rate. Under rapid water-quenched conditions, complex partitioning of the alloying elements between γ and γ' phases was observed. Atom probe tomography on samples subjected to slower cooling rates showed different partitioning behavior compared to that of water-quenched samples and the presence of secondary γ' precipitates in the samples subjected to a cooling rate of 1 K s^{-1}. *Published by Elsevier Science Ltd on behalf of Acta Materialia Inc.*

Keywords: Welding; Transmission electron microscopy (TEM); Atom probe; Nickel base superalloys

1. INTRODUCTION

There is a need to develop welding processes to join directionally solidified (DS) and single crystal (SX) nickel base superalloys for efficient reuse and reclamation of used and failed components [1]. Previous work shows that it is possible to weld DS and SX alloys using electron (EB) and laser beam (LB) welding processes. However, for successful crack-free welds, both DS and SX alloys are welded either with a high preheat temperature (~773 K) during electron beam welding or with pulsed mode in laser beam welding. A high preheat temperature leads to slow cooling (~1 K s^{-1}) from the melting temperature that in turn leads to reduced stresses and thereby avoids the formation of weld cracks. In contrast, pulsed mode laser welding leads to low heat-input and therefore rapid cooling rates (>100 K s^{-1}). Such large variations in weld cooling rates influence the final weld microstructure.

The microstructures in such welds were previously characterized with transmission electron microscopy (TEM) and atom probe field ion microscopy (APFIM) in commercial single crystal nickel–base superalloys [2, 3]. These studies showed that the microstructure obtained from an electron beam weld of a PWA-1480 alloy was similar to that of the base metal (see Fig. 1). The microstructure contained coarse eutectic γ and γ'($L1_2$-ordered) phases, and cuboidal γ' precipitates within the γ matrix. Atom probe analysis showed the phase compositions were also similar to that of base metal [2]. In pulsed laser welds made on CMSX-4 alloys, the microstructure was different from that of base metal. The weld metal did not contain the eutectic γ and γ' microstructure but contained fine (~50 nm) γ' precipitates distributed within the γ phase. Atom probe analysis revealed that the characteristics of elemental partitioning were different from those of base metal [3]. In addition, concentration profiles showed large diffusion profiles of Cr in the γ phase ahead of the γ–γ' interface. Such diffusion profiles are expected to have a large influence on the high-temperature properties. These results indicated that there is a strong relationship between weld cooling rate and the precipitation of γ' precipitates from the γ phase. However, it cannot be quantitatively analyzed, as it is difficult to accurately measure the weld cooling rates in the EB and LB welding processes. Moreover, the results were from two different alloy compositions. The effects due to alloy composition and cooling rate cannot be distinguished without making some assumptions.

† To whom all correspondence should be addressed. Tel.: +1-865-574-4806; fax: +1-865-574-4928.

E-mail address: babuss@ornl.gov (S. S. Babu)

1359-6454/01/$20.00 Published by Elsevier Science Ltd on behalf of Acta Materialia Inc.
PII: S1359-6454(01)00314-7

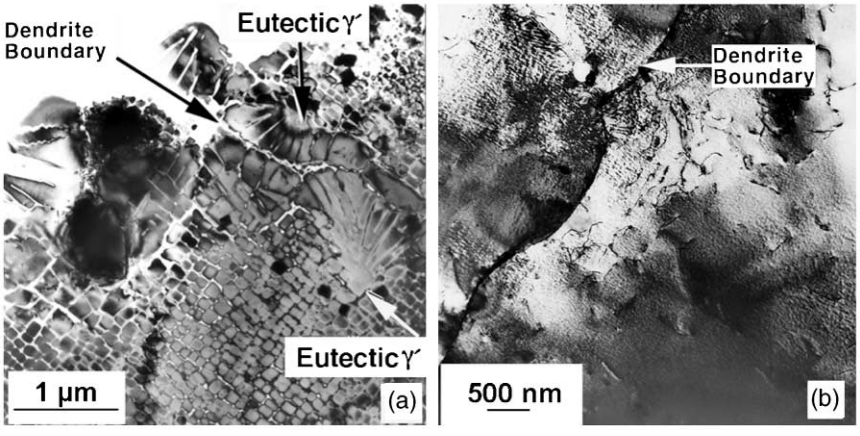

Fig. 1. Transmission electron micrograph from the weld metal region of (a) PWA-1480 electron beam weld and (b) CMSX-4 laser beam weld.

The precipitation of the γ' phase from the γ phase has been previously studied in various Ni–base alloys [4–12]. Some of this research considered the formation of γ' precipitate during different cooling rates [8, 9, 12] and noticed an increase in the number density and decrease in the size of the precipitates with increased cooling rates. Mackay and Nathal [8] cooled a Ni–Al–Mo–Ta alloy from the single-phase γ region using forced-air cooling and oil quenching. The slow forced air-cooling led to formation of coarser γ' precipitates compared to those after oil quenching [9]. The cooling rates were not quantified and the details of the γ' composition were not studied. Jackson *et al*. [12] found that the size of the γ' precipitates decreased from 72 to 37 nm as the cooling rate increased from 0.08 to 0.33 K s^{-1} in a Ni–13.0 at.% Al alloy [12]. However, the cooling rates used were slower than those of a typical weld.

Other research on γ' phase precipitation from the γ phase focused on understanding the mechanism of nucleation and growth in low-supersaturated Ni–Al [4–6] and Ni–Cr–Al systems [11]. These researchers showed that the initial decomposition occurs by nucleation and growth and the subsequent growth occurs by coarsening mechanisms. Wendt and Haasen *et al*. stopped the decomposition of the γ phase by quenching. After quenching and isothermal aging at high temperatures, they observed the early stages of nucleation and growth and found that the γ' precipitates were close to equilibrium composition from early stages [6]. Recent research by Schmuck *et al*. [11] showed a similar mode of decomposition with the use of three-dimensional atom probe in a Ni–Cr–Al system. Both the alloys studied by Wendt and Haasen [6] and Schmuck *et al*. had low supersaturation of the γ' forming elements, which allowed the γ phase to be retained at room temperature and the subsequent isothermal transformation to be studied at high-temperature. However, in commercial alloys, the γ phase cannot be retained to room temperature due to the high concentrations of γ' phase forming elements such as Al and Ti. Using APFIM, Blavette *et al*. [7, 10] showed that the decomposition of the γ phase in most commercial nickel base superalloys could not be stopped due to the large driving force for the precipitation of the γ' phase. However, the morphology of the γ' precipitates that formed during rapid cooling conditions was not studied. Early work on the microstructure and precipitation sequences in rapidly solidified nickel superalloys showed some indications of phase separation without ordering [13].

Based on the previous work, the goals of this work are as follows: (1) Study the precipitation kinetics in CM247DS alloys at typical weld metal cooling rates (0.17 to 75 Ks^{-1}) and in the water-quenched condition; (2) characterize the number density, size, and morphology of the γ' precipitates; (3) measure the composition of these γ' precipitates and the γ matrix using atom probe field ion microscopy and atom probe tomography (APT); and (4) apply computational thermodynamics and kinetic calculations to model the precipitation of the γ' phase from the γ phase during continuous cooling conditions.

2. EXPERIMENTAL

The composition of the CM247DS alloy is given in Table 1. In this investigation, rod samples (6.3-mm diameter) were machined from the castings after a standard heat treatment involving slow heating solutionizing temperature (~1585 K) and isothermal heat-treatment at 1413 K after a step cool to 1273 K. Controlled heat treatments were performed in a Gleeble® thermomechanical simulator. The samples were solutionized at 1573 K (±10 K) for 5 min and were cooled at different rates (0.17, 1, 10, and 75 K s^{-1}). The solutionizing temperature was based on the γ' solvus as measured by differential thermal analysis. During these heat treatments, the diameter of the samples was continuously monitored using dilatometric techniques. For comparison and evaluation, the diameter change of a pure nickel sample was also

Table 1. Composition of CM247DS alloy

	Cr	Co	Al	Ti	Nb	Mo	Ta	W	C	Ni
at. %	9.12	9.05	12.1	1.0	0.06	0.37	1.05	3.06	0.40	Balance
wt. %	8	9	5.5	0.8	0.1	0.6	3.2	9.5	0.08	Balance

measured under similar conditions. The measured data from pure nickel samples were compared with the published data [14]. The CM247DS samples were also water quenched from 1573 K to investigate the stability of γ and γ' phases during rapid cooling conditions.

Microstructural analyses were performed by TEM, APFIM [15] and atom probe tomography (APT) [16, 17]. Transmission electron microscopy was performed in a Philips-CM12 transmission electron microscope. The APFIM and APT characterizations were performed on as-received base metal, 1 K s^{-1}, 75 K s^{-1} and water-quenched samples. Field ion microscopy was performed at 50–60 K with neon as the imaging gas. The APFIM analyses were performed at 20% pulse fraction and a pulse repetition of 1500 Hz with a residual neon gas pressure of 3×10^{-7} Pa.

3. RESULTS

3.1. Dilatometry

The relative change in radius of the pure nickel rod sample was monitored during cooling from 1573 K at 10 and 75 K s^{-1}. The coefficients of thermal expansion calculated from these data were in agreement with the published data [14, 18]. With the confidence of measurement accuracy, the dilatation of CM247DS samples was measured at different cooling rates (1, 10 and 75 K s^{-1}) during cooling from 1573 K. The relative changes in radius measured under these conditions were compared with those of pure nickel samples (Fig. 2). The relative changes in radius with temperature for CM247 samples were different from those of pure nickel samples. The samples cooled at 1 K s^{-1} and 10 K s^{-1} both showed an abrupt slope change at ~1433 K. The sample cooled at 10 K s^{-1} showed another slope change at ~1333 K. However, the sample cooled at 75 K s^{-1} did not show any abrupt slope change and the data show a gradual change with temperature. The above changes are qualitatively attributed to the combined effect of changes in volume fraction and differences in the coefficient of thermal expansion of γ and γ' phases that form during these cooling conditions. These changes are specific to CM247DS alloys as supported by the absence of such changes in the pure nickel sample. Since the lattice parameters of the γ and γ' phases in CM247DS alloy are not known as a function of temperature, the above data could not be converted into real volume fraction and interpreted quantitatively.

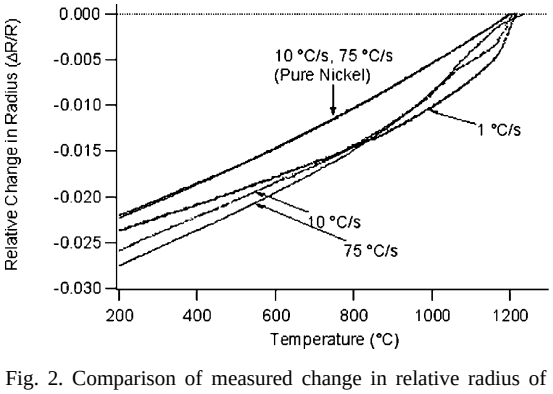

Fig. 2. Comparison of measured change in relative radius of CM247DS alloy rod with temperature while cooling from solutionizing temperature (1573 K) at three different cooling rates. The measured relative radius changes were also compared with that of pure nickel for similar cooling rates.

3.2. Transmission electron microscopy

Transmission electron micrographs of heat-treated samples are compared with as-received samples in Fig. 3. All the micrographs were taken near to the [0 0 1] zone axis, therefore, permitting a direct comparison of the γ' precipitate size. The samples subjected to cooling at a rate of 0.17 K s^{-1} [Fig. 3(b)] consist of coarser cuboidal γ' precipitates than in the as-received condition. The morphology of these precipitates shows indication of coarsening. The samples subjected to a cooling rate of 1 K s^{-1} [Fig. 3(c)] showed cuboidal γ' precipitates and some irregularly shaped precipitates. In addition to the primary γ' precipitates (~200 nm), there were some fine secondary γ' precipitates (~20 nm). These fine secondary precipitates are shown in Fig. 4(a). The sample subjected to continuous cooling at 10 K s^{-1} [Fig. 3(d)] showed finer γ' precipitates. However, there were no secondary γ' precipitates. The γ' precipitate size decreased [see Fig. 3(e)] and the number density increased at a cooling rate of 75 K s^{-1}. In addition, the morphology of the γ' precipitates tends to exhibit irregular instead of cuboidal shape. In the water-quenched condition, the number density of the γ' precipitates increased and their size decreased [see Fig. 3(f)] and their shape became more spherical. The morphology of some γ' precipitates showed some interconnectivity as indicated by arrows in Fig. 4(b). However, these images could be artifact due to superimposed images of precipitates at different thickness. The number density and size of the γ' precipitates are quantified in Fig. 5. As the cooling rate increased from 0.17 to 75 K s^{-1}, the number density increased with a corresponding decrease in the size. The difference in the number

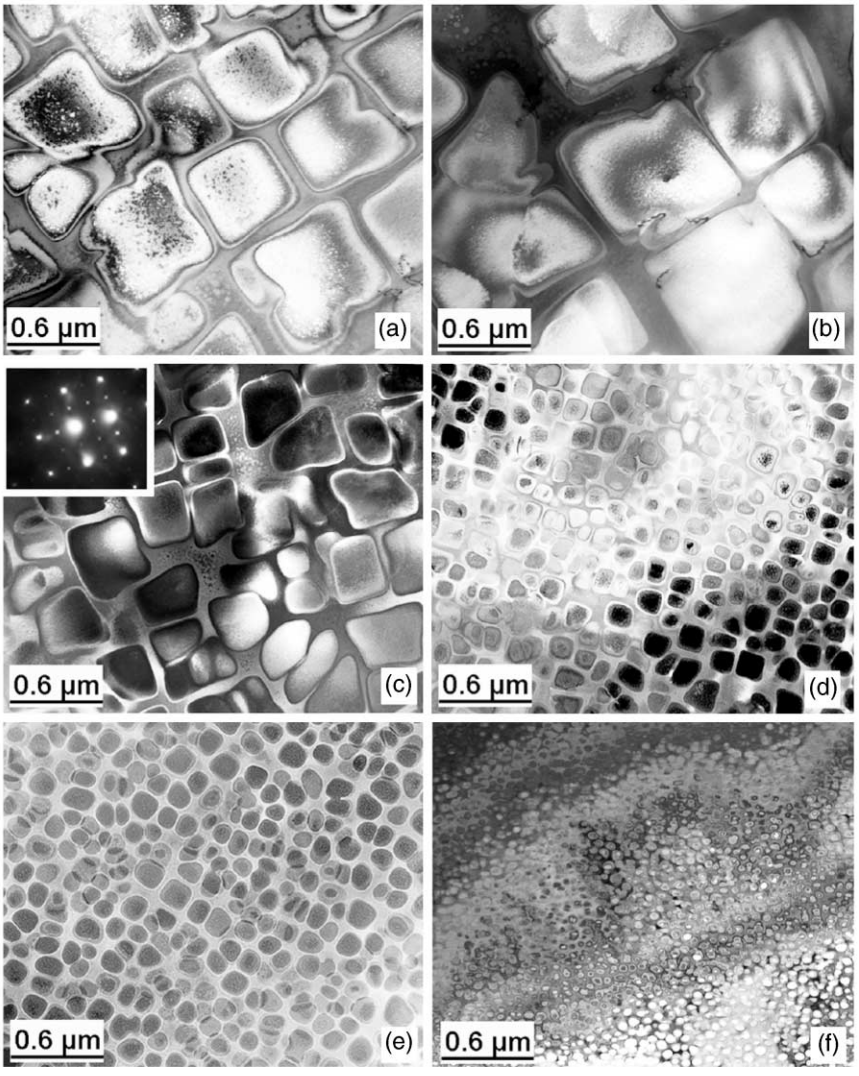

Fig. 3. Transmission electron micrographs ([0 0 1] zone axis) of (a) as received heat-treated CM247DS sample and the alloy subjected to solutionizing at 1573 K for 5 min and cooled at different rates. Microstructures obtained at (b) 0.17 K s^{-1}; (c) 1 K s^{-1} (insert — diffraction pattern from the same sample), (d) 10 K s^{-1}, (e) 75 K s^{-1}, and (f) water-quenched condition.

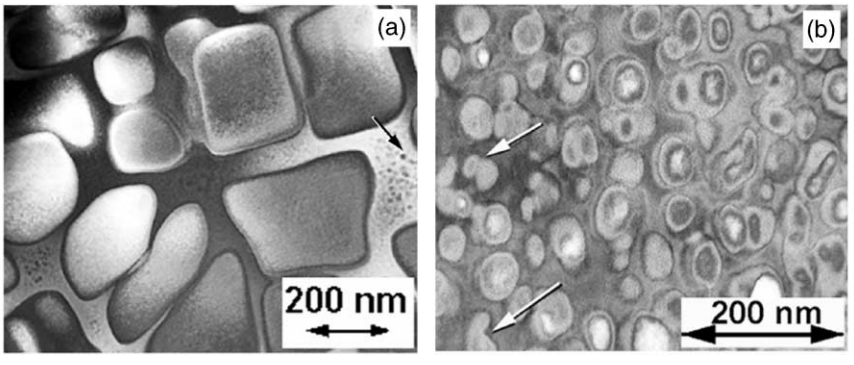

Fig. 4. High-magnification transmission electron micrograph from the samples (a) subjected to 1 K s^{-1} showing the presence of secondary γ' precipitates (marked by an arrow) and (b) water-quenched condition showing fine γ' precipitates and complex morphology (shown by arrows) of the same.

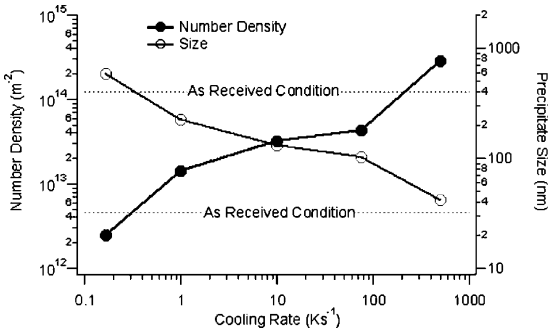

Fig. 5. The measured variation of number density and precipitate size as a function of cooling rate.

density of the γ' precipitates between the samples cooled at 10 and 75 K s^{-1} was not large. However, the number density of the γ' precipitates increased by an order of magnitude in the water-quenched sample compared to that of samples cooled at 75 K s^{-1}. To evaluate this sudden increase in number density and the complex shape of the γ' precipitates, atom probe field ion microscopy and atom probe tomography were used to measure the fine scale partitioning between the γ and γ' phase in the water-quenched sample. These measurements were compared with similar measurements from samples cooled at 75 K s^{-1}, 1 K s^{-1} and the base metal.

3.3. Atom probe field ion microscopy and atom probe tomography

Atom probe concentration profiles from the water-quenched sample are shown in Fig. 6. The profiles show Cr-enriched γ and Al-enriched γ' phases. In addition, Co was found to partition to γ phase and Ta to the γ' phase. These results are in agreement with expected partitioning trends. However, some interesting observations were made with respect to partitioning of Ti, W and Co. A Co-enriched region was detected within the γ' phase. The partitioning characteristics of Ti and W were complex. From previous work [2, 3], it is expected that Ti would partition to the γ' phase and W to the γ phase. The concentration profiles indicated Ti and W enriched regions within both the γ and γ' phases. The average composition of γ and γ' phases from these concentration profiles are tabulated in Table 2 and indicate that the partitioning of Al, Cr, Co and Ta between the γ and γ' phases is significant, whereas the partitioning of Ti and W was not significant.

Further analyses of water-quenched samples were performed with APT to determine the partitioning characteristics as well as the γ' morphology. The Cr atom map is shown in Fig. 7(a). The atom map shows complex γ' phase morphology with no regular cuboidal or spherical morphology. Some of the γ' precipitates had both flat and curved interfaces with the γ phase. The concentration profiles were measured from a selected volume within the data as shown in Fig. 7. The concentration profiles indicate Cr-enriched γ regions and Al-enriched γ' regions. Similar to one-dimensional APFIM results, the concentration profile indicated complex partitioning of the other alloying elements. Small Co-enriched regions were observed within the γ' phase and W and Ti did not partition exclusively either to the γ or γ' phases. In agreement with previous observations, Ta seems to partition to the γ' phase. An Al-enriched region was also observed within the γ phase. An important observation is that Cr and Co do not show any enrichment near the γ–γ' interface. The average compositions of the γ and γ' phases from the data shown in Figs 6 and 7 are summarized in Tables 2 and 3.

The composition of the γ' phase measured from APT is comparable to that measured from APFIM. Both the techniques showed the partitioning of carbon to the γ' phase and the concentrations of other elements were in agreement with each other within the limits of error. However, the composition of the γ phase measured from APT was different from that of APFIM. This is attributed to the uncertainty of the APFIM analyses direction with respect to γ and γ' interface. Due to the thin film like nature of γ phase in this sample, such errors are expected in one-dimensional atom probe analysis. In APT analyses, the axis of the selected volume was chosen to be perpendicular to the interface plane.

The morphology of the γ phase in two regions A and B shown in Fig. 7(a) was evaluated. The iso-concentration surface of Cr at region A shows that the γ phase is continuous along the neighboring γ' precipitates. This indicates that the γ' precipitates on either side of the γ phase in A are interconnected to each other. This interconnected morphology supports the suggested morphology based on observations in the TEM. The concentration profiles in Fig. 7(b) did not indicate any excessive enrichment of chromium (maximum of 12 at.%) in this thin γ phase. In contrast, the γ phase in region B is continuous and the γ' phase on either side appears to be separate precipitates.

Atom probe tomography results from samples that were subjected to 75 K s^{-1} cooling rates are presented in Fig. 8. The Cr atom map showed γ' precipitates distributed within the γ phase. Similar to the water-quenched samples, the morphology of the γ' phase was irregular, i.e., neither cuboidal nor spherical. The concentration profiles [Fig. 8(b)] from a selected volume did not show any Co-enriched regions within the γ' phase. The partitioning characteristics of Cr, Al, and Ta were similar to the expected behavior (see Table 2). The partitioning tendency of Ti to the γ' phase was slightly evident. Similar to water-quenched samples, W did not partition either to the γ or γ' phases. The thin γ region (~8 nm) was found to be enriched in Cr (maximum of 36 at.%). This is more evident in the Cr iso-concentration surface shown in Fig. 8(c). The plots show that the γ' precipitates are well separated by γ phase. In agreement with TEM

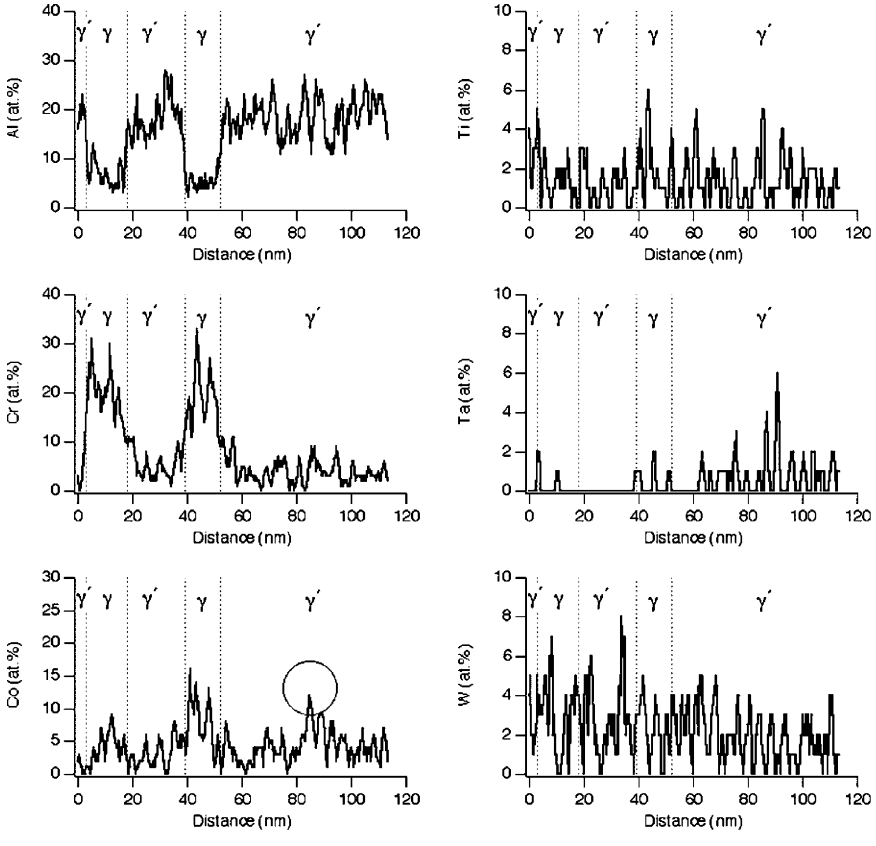

Fig. 6. Atom probe concentration profile across γ and γ' phases in the CM247DS sample subjected to solutionizing and water-quenching treatment.

Table 2. Average composition (at.%) of the γ phase measured by APFIM and APT. The balance of all compositions is nickel

Cr	Co	Al	Ti	Ta	W	C
γ composition from waterquenched sample measured by APFIM						
20.38±0.76	4.3±0.37	6.62±0.4	1.36±0.13	0.16±0.06	2.84±0.27	0
19.21±0.95	8.15±0.67	5.5±0.33	1.95±0.23	0.39±0.1	2.29±0.21	0
γ composition from water quenched sample measured by APT						
14.05±1.23	13.85±1.47	7.59±0.76	0.93±0.37	0.08±0.08	3.84±0.83	0.09±0.09
13.68±1.14	12.18±1.31	7.24±1.21	1.07±0.36	0	3.42±0.47	0
16.96±2.16	14.37±1.32	4.87±0.95	1.07±0.48	0	3.96±0.86	0
γ composition from sample cooled at 75 K/s measured by APT						
24.36±4.10	15.72±1.71	6.48±1.17	1.42±0.33	0.27±0.27	3.73±0.44	0
26.93±0.82	16.13±0.53	5.25±0.62	1.13±0.21	0	2.32±0.31	0
24.61±0.79	14.71±0.48	5.33±0.50	1.58±0.2	0.08±0.04	2.86±0.27	0
γ composition from sample cooled at 1 K/s measured by APT						
19.31±0.78	13.40±0.69	3.94±0.39	1.30±0.22	0.0	3.00±0.34	0
19.24±0.79	13.73±0.69	5.39±0.45	1.42±0.24	0.0	2.96±0.34	0
γ composition from base metal sample measured by APT						
21.85±0.43	16.02±0.38	3.58±0.19	1.36±0.12	0.01±0.01	3.34±0.19	0.06±0.03

observations, the APT results did not show any interconnected γ' morphology.

A field ion microscopy (FIM) image of samples subjected to 1 K s^{-1} cooling rate is shown in Fig. 9 and indicates the presence of primary γ' precipitates, γ phase and also small secondary γ' precipitates. The morphology and composition of these phases were characterized with APT. The Cr atom map from a large data set with a primary γ' precipitate, γ phase and secondary γ' precipitate is shown in Fig. 10(a). The average compositions of these phases are given in Tables 2 and 3. The atom maps showed a small Cr-enriched region in the γ' phase [marked as "B" in Fig. 10(a)]. The local composition of this region was found to be Ni–15.16±0.55% Al (at.%)–6.01±0.36% Cr–5.24±0.34% Co–3.04±0.26% W–3.70±0.29% Ti–0.37±0.08 B–0.19±0.07% C–0.14±0.06 Ta. The morphology from APT analysis indicated that these regions may be segregated within the γ' phase. A selected volume (marked as "A") was further analyzed to evaluate the morphology and the composition of the secondary γ' precipitates. Three-dimensional

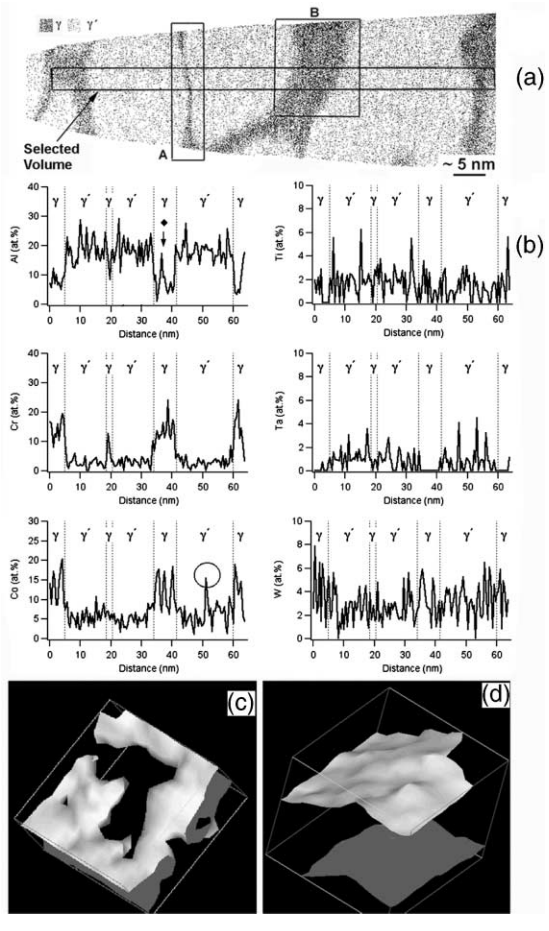

Fig. 7. (a) Chromium atom map obtained from APT analysis from CM247DS sample in the water-quenched condition. (b) Atom probe concentration profiles obtained from the selected volume region shown in (a). 15 at.% Cr iso-concentration of (c) region A and (d) region B showing the γ phase morphologies.

representation of the Cr atom map of region "A" is shown in Fig. 10(b). The 15 at.% Cr iso-concentration surfaces are shown in Fig. 10(c) and indicate that the secondary γ' precipitates are spherical or ellipsoidal in nature. The sizes of these precipitates were smaller than those observed in the water-quenched condition. However, these precipitates were isolated and did not show any interconnectivity. The concentration profiles across these precipitates are shown in Fig. 10(d). The profiles indicate that the γ phase in between two secondary γ' precipitates was highly enriched in Cr. The average composition of the primary and secondary γ' phases and the γ phase are summarized in Tables 2 and 3. The composition of primary and secondary γ' precipitates appears to be similar, except for reduced Al concentration in the secondary γ' precipitates. The γ composition from this sample was different from other samples. For example, the Cr concentration in the γ phase was approximately ~19 at.% compared to that of ~25 at.% in the sample cooled at 75 K s^{-1}. Similar to other samples, the partitioning of Ti and W were not observed.

The APT results from the as-received base metal sample are shown in Fig. 11. The Cr atom maps showed the presence of γ phase sandwiched between two γ' precipitates. As the size of the γ' precipitates is larger than the volume of analysis, the morphology of the whole γ' precipitate cannot be obtained. The atom maps showed a small step (along the γ–γ' interface marked by A and B) on the γ' precipitates. The origin of this step is not clear, however, similar step like features are indeed observed in the transmission electron microscopy [see Fig. 3(a)]. The concentration profiles across the γ and γ' phases in the selected volume are shown in Fig. 11(b). The Co and Al concentration profiles did not show any large concentration gradients within the γ' phase. However, the Cr

Table 3. Average composition (at.%) of the γ' phase measured by APFIM and APT. The balance of all compositions is nickel

Cr	Co	Al	Ti	Ta	W	C
γ' composition from water quenched sample measured by APFIM						
4.31±0.32	2.89±0.31	19.02±0.6	0.96±0.12	0.0	2.87±0.26	0.15±0.05
3.69±0.18	4.09±0.2	18.52±0.31	1.35±0.09	0.73±0.07	1.91±0.09	0.04±0.01
γ' composition from water quenched sample measured by APT						
2.43±0.28	5.3±0.45	18.43±0.87	1.82±0.31	1.14±0.17	2.53±0.28	0.08±0.06
2.63±0.30	4.80±0.38	18.74±0.83	1.89±0.25	0.82±0.16	2.49±0.23	0.03±0.03
2.44±0.25	5.91±0.53	18.08±0.6	1.10±0.17	0.79±0.2	3.15±0.27	0.06±0.05
γ' composition from sample cooled at 75 K/s measured by APT						
2.93±0.46	4.92±0.67	18.25±0.92	1.31±0.25	2.51±0.32	3.09±0.4	0
4.29±0.35	6.42±0.48	19.08±0.64	1.47±0.2	2.5±0.24	1.93±0.23	0
3.59±0.28	6.62±0.43	18.43±0.61	1.80±0.23	1.80±0.23	2.79±0.25	0
4.06±0.35	6.21±0.30	17.59±0.55	2.00±0.22	1.92±0.16	2.18±0.30	0
Primary γ' composition from sample cooled at 1 K/s measured by APT						
2.85±0.17	5.46±0.23	17.28±0.38	1.43±0.16	0.14±0.04	3.42±0.18	0.02±0.01
2.82±0.17	5.57±0.23	17.15±0.38	1.39±0.12	0.26±0.05	3.53±0.19	0.01±0.01
2.98±0.25	5.92±0.35	17.48±0.56	1.14±0.16	0.09±0.04	3.82±0.28	0
2.93±0.13	6.10±0.19	16.90±0.25	1.52±0.09	1.55±0.09	2.55±0.12	0
Secondary γ' composition from sample cooled at 1 K/s measured by APT						
3.27±0.29	5.89±0.39	14.92±0.59	1.09±0.17	0.03±0.03	3.68±0.31	0
γ' composition from base metal sample measured by APT						
3.18±0.08	6.12±0.25	16.77±0.38	1.20±0.11	0.11±0.03	3.89±0.2	0.03±0.02
3.29±0.18	6.05±0.24	16.95±0.38	1.28±0.11	0.15±0.04	3.64±0.19	0.01±0.01
2.82±0.17	5.81±0.24	17.23±0.39	1.44±0.12	0.16±0.04	3.74±0.2	0.03±0.02
3.15±0.02	6.11±0.02	16.28±0.05	1.38±0.01	1.47±0.02	2.76±0.02	0

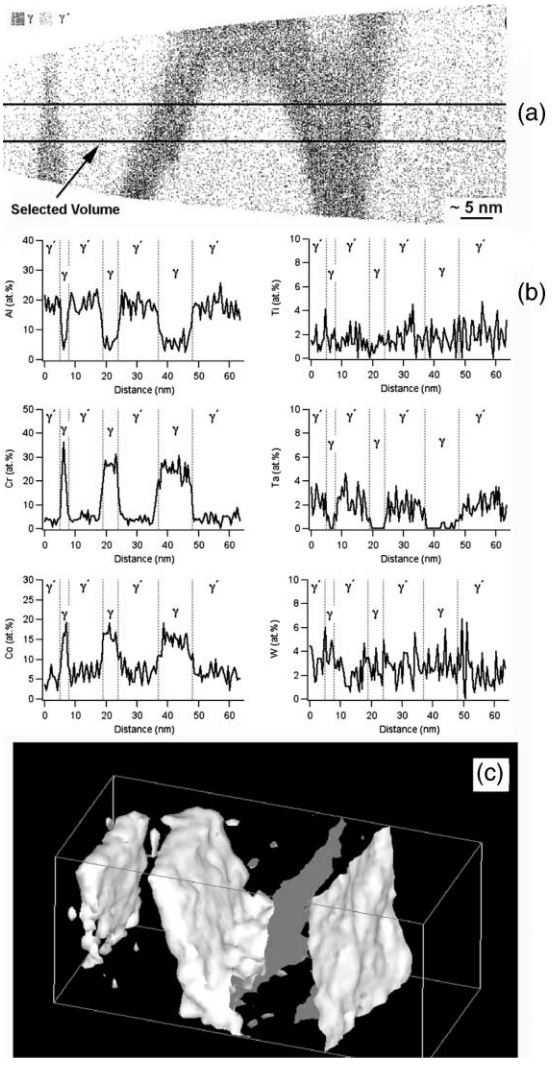

Fig. 8. (a) Chromium atom map obtained from APT analysis from CM247DS sample continuously cooled at 75 K s^{-1}. The concentration profiles were obtained from the selected volume region shown in (b). (c) Morphology of the γ and γ' precipitates analyzed with 15 at.% Cr iso-concentration surfaces.

concentration profiles indicated a very small concentration gradient near the γ–γ' interface (marked as AB). The compositions of the γ and γ' phases are compared with other samples in Tables 2 and 3. Again, Ti and W do not show any preferred partitioning between the γ and γ' phases.

4. DISCUSSION

The observed microstructural evolution can be explained by nucleation and growth theories. The observed increase in the number density for the γ' precipitates with the cooling rate suggests that the decomposition of the γ phase occurred under large undercooling. Under large undercooling below the equilibrium instability temperature, the driving force for the nucleation of the γ' phase is expected to

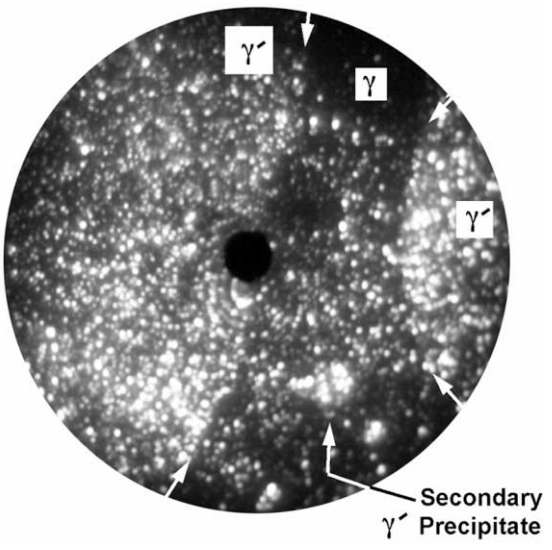

Fig. 9. FIM image from the CM247DS sample cooled at 1 K s^{-1} showing the presence of primary and secondary γ' precipitates. The white arrows mark the two γ/γ' interphase boundaries.

increase rapidly, as a result, the nucleation rate of the γ' precipitate per unit volume will increase. The results of the calculation of the driving force using a commercial thermodynamic software [19] for a Ni–12.1 at.% Al–9.05% Co–9.12% Cr system with a thermodynamic database† [20] are shown in Fig. 12. The calculations indicate a monotonic increase in the driving force below the instability temperature of 1272 K. This increase in driving force should lead to a continued increase in the nucleation rate of the γ' phase, provided there are no large changes in interfacial surface energy (between the γ and γ' phases) and elastic strain energy of the γ' precipitates. The continued increase in nucleation rate should manifest itself as an increased number density of γ' precipitates. This hypothesis is supported by the microstructural observation shown in Fig. 3. This result is also in agreement with previous research [8, 9, 12].

An attempt was made to describe the nucleation and growth of γ' precipitates using available theoretical equations and computational tools for the above Ni–Al–Cr–Co alloy. The homogenous nucleation rate (I_{vol}) of the γ' phase from the γ phase was calculated from

$$I_{vol} = A\exp\{\frac{-\Delta G^*}{kT}\}\exp\{\frac{-Q}{kT}\}, \qquad (1)$$

where A is a pre-exponential factor is assumed to be 1×10^{30}, T is the temperature in kelvin, ΔG^* is the

† Thermodynamic calculations could not consider all the elements in this alloy system due to the limitations of the thermodynamic database.

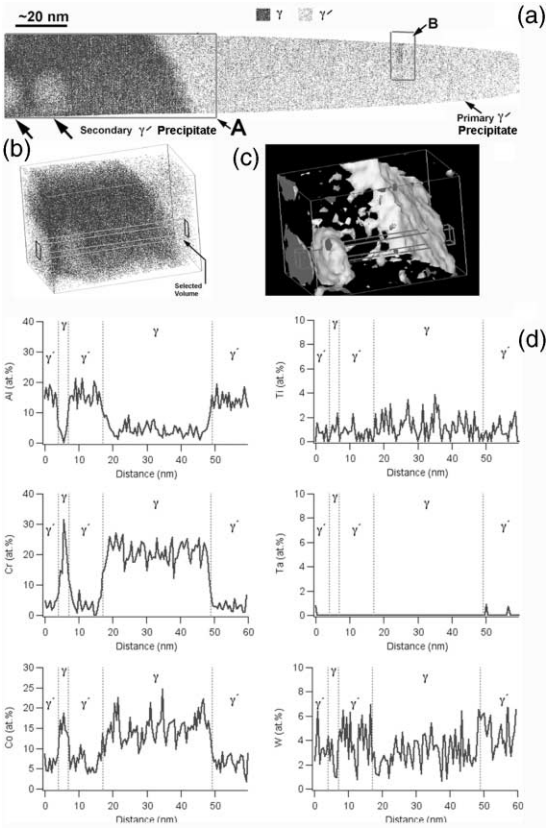

Fig. 10. (a) Chromium atom map from the CM247DS sample cooled at 1 K s^{-1} showing both coarse primary and fine secondary γ' precipitates; the rectangular region marked "B" was enriched in Cr; (b) three dimensional reconstruction of selected volume marked "A" in (a); (c) 15 at.% Cr iso-concentration surface showing the presence of secondary γ' precipitates; (d) concentration profiles from a selected volume shown in (b) which intersects the secondary γ' precipitates, γ phase and primary γ' precipitate.

activation energy for nucleation and Q is the activation energy for self-diffusion. The activation energy for nucleation is calculated from

$$\Delta G^* = \frac{16\pi\sigma^3}{3[\Delta G_{\text{vol}} - \Delta G_{\text{strain}}]^2} \tag{2}$$

where ΔG_{vol} is the driving force for nucleation of γ' precipitates per unit volume, ΔG_{strain} is the strain energy per unit volume of γ' precipitates and σ is the surface energy per unit volume (assumed to be 0.02 J m^{-2}). The ΔG_{strain} is calculated from the formulation given by [11]:

$$\Delta G_{\text{strain}} = 3.8\mu\delta^2, \tag{3}$$

where μ is the shear modulus (1.2×10^{11} N m^{-2}) and δ is the lattice misfit (0.07%). The activation for the self-diffusion is related to the melting point of the alloy as given by [21]

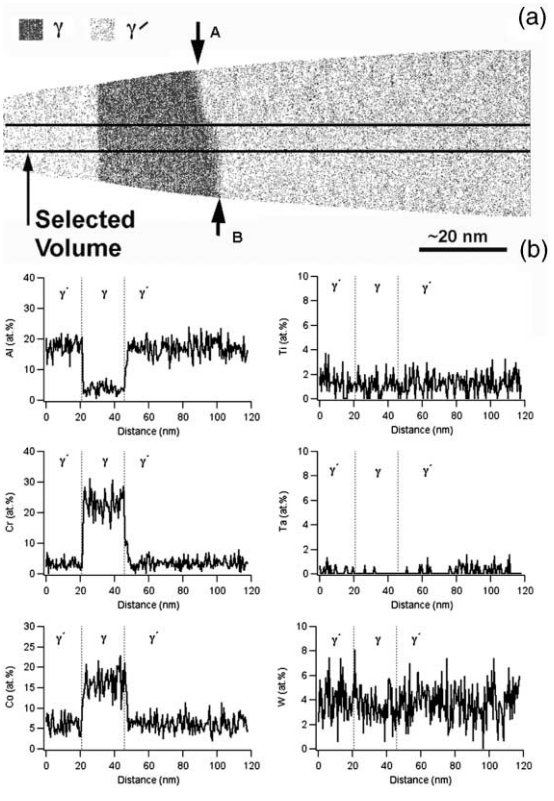

Fig. 11. (a) Chromium atom map from the CM247DS base metal showing γ' and γ phases; (b) concentration profiles obtained through the selected volume shown in (a).

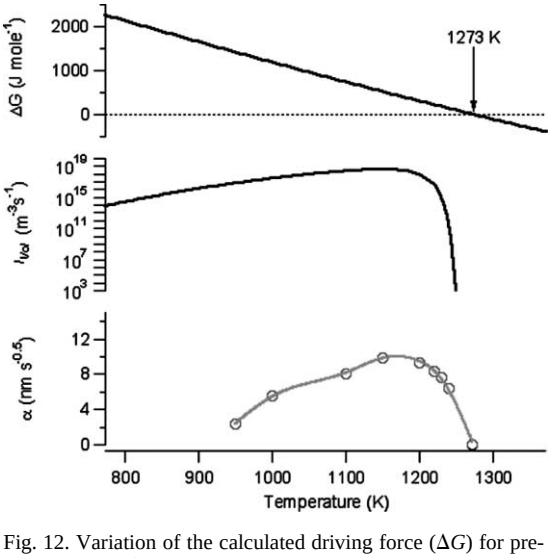

Fig. 12. Variation of the calculated driving force (ΔG) for precipitation of γ' phase from the γ phase, the nucleation rate (I_{vol}) of the γ' phase, and the parabolic growth rate (α) of the γ' phase in a Ni–Al–Cr–Co system as a function of temperature.

$$Q_{\text{mobility}} = \frac{142.188T_{\text{melting}}}{6.023\times10^{23}} \tag{4}$$

From the above relations, and the driving force for

the γ' phase [shown in Fig. 12(a)] the nucleation rate of the γ' phase as a function of temperature can be calculated and the results are shown in Fig. 12(b). Note that these calculations ignore the effect of capillarity. The results show that the nucleation rate increases rapidly with large undercooling below the equilibrium instability temperature. However, below a certain temperature, the nucleation rate decreases slightly due to the reduction in atomic mobility.

It is important to consider the growth of the γ' precipitates to evaluate the overall transformation kinetics in these alloys. The growth rate calculations were performed using commercial DicTra software [22]. In this simulation, a γ phase element of 1 μm size is considered to avoid overlap of diffusion fields and subsequent reduction in growth rate. Isothermal growth of γ' precipitates into the γ phase at various temperatures was simulated assuming one-dimensional diffusion in the γ phase. Since the calculations cannot model diffusion in the γ' phase, the diffusion within the γ' phase is ignored. Therefore, the growth rate is essentially controlled by diffusion of Ni, Al, Cr, and Co within the γ phase. The effects of strain and surface energy on the interface composition were ignored. Initial simulation attempts led to some difficulties due to the presence of steep concentration gradients ahead of the γ–γ' interface within the γ phase. To alleviate this problem, the γ' was allowed to form as the γ phase was cooled from instability temperature to the isothermal aging temperature at a cooling rate of 100 K s^{-1}. This modification allowed the concentration gradients to be modest and allowed for successful calculation of growth rates of the γ' phase in the γ matrix. The calculated rate of interface movement is represented in the form of parabolic thickening rate (α) in Fig. 12(c). The relation between α and the thickness of the γ' phase (q) and the time spent (t) at the isothermal temperature is given by:

$$q = \alpha t^{0.5} \tag{5}$$

The results from Fig. 12 show that for large undercooling, the nucleation of the γ' phase can be sustained, the growth rate of the γ' phase will decrease rapidly below 1150 K. Therefore, the kinetics will be retarded at large undercooling below 1000 K.

The calculated results also indicate that at slow cooling rates, the nucleation rate will be sluggish and most of the transformation will be controlled initially by growth and subsequently by coarsening, therefore large γ' precipitates will be promoted. This is observed in samples cooled at 0.17 K s^{-1}. In the case of samples cooled at a higher cooling rate, most of the transformation will occur at a lower temperature where both nucleation and growth rates are higher. This condition will promote rapid transformation and a fine number density of γ' precipitates as seen in the samples cooled at 10–75 K s^{-1}.

In the samples cooled at 1 K s^{-1}, a bimodal dual size of γ' precipitates was observed; large γ' precipitates and small secondary γ' precipitates within the γ phase. At this slow cooling rate, a substantial amount of the γ' phase nuclei may form and grow. However, the growth rate of these precipitates reduces due to overlap of the diffusion field ahead of the interface. This is a normal consequence of diffusion controlled growth. This leads to an Al-depleted region near the growing γ' phase interface, and the γ phase region far from the interface may have the bulk or slightly lower of the Al concentration. This γ phase region may nucleate more γ' precipitates with different compositions as the sample cools. These modes of growth, however, need to reject Cr into the γ phase. Therefore, a highly Cr-enriched γ phase is expected near the secondary γ' precipitates. The APT results showed the Al-concentration of the secondary γ' precipitates was less than that of the primary γ' precipitates (see Table 3) and also the presence of Cr-enriched γ phase near the interface (see Fig. 10). Further work is necessary to identify the temperature at which the secondary γ' precipitates form and grow, through *in-situ* neutron and X-ray diffraction studies [23].

The rapid increase in number density of γ' precipitates and the complex interconnected γ' morphology in the water-quenched condition could not be rationalized based on nucleation and growth mechanism. It is possible to argue that the observed interconnectivity is due to the impingement of separately nucleated γ' precipitates. If that is the case, the γ phase region between these γ' precipitates must be enriched in elements such as Cr and Co due to diffusional field overlaps. The concentration of the thin γ phase (~20 nm distance from the start) between the interconnected γ' precipitates [see Figs 8(b) and 10(b)] does not show such enrichments (~12 at.% Cr). However, samples cooled at a rate of 75 K s^{-1} and 1 K s^{-1}, exhibited enrichment up to 35 at.% Cr in the γ phase region between γ' precipitates. Based on this observation, it is concluded that the interconnected γ' morphology is not due to impingement of separately nucleated γ' precipitates. Therefore, the origin of interconnected γ' morphology remains to be explained.

Ordering and subsequent phase separation is one of the mechanisms by which a γ phase can decompose into a mixture of γ phase and $L1_2$-ordered γ' precipitates. Numerous treatments of such a mode of transformation have been documented in the literature for binary alloys [24–28]. From these works, four instabilities govern overall transformation: phase separation of the γ phase, ordering of the γ phase, phase separation of $L1_2$-ordered phase and disordering of $L1_2$-ordered phase, as shown in a schematic diagram for binary alloys in Fig. 13. Based on these theories, at large undercoolings, the γ phase can order (congruently) without any compositional changes and then undergo a phase separation through compo-

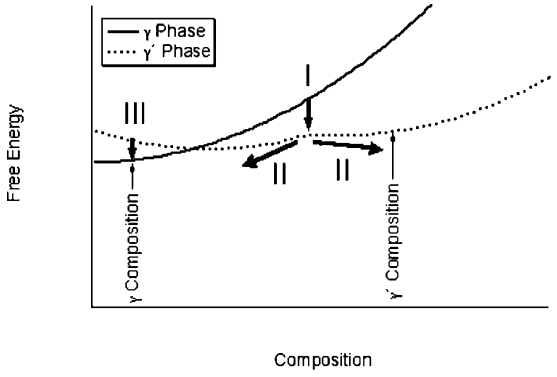

Fig. 13. Schematic illustration of a hypothetical free energy-composition diagram for a binary alloy that might undergo a transformation through congruent ordering and subsequent phase separation and instantaneous disordering.

sitional waves. Once the regions with lower amplitude concentrations reach a minimum level, that region can undergo instantaneous disordering. This transformation path (*I*→*II*→*III* in Fig. 13) may allow for complex interconnected γ' precipitates. It is important to note that congruent ordering is possible at and below the T_0 temperature (at this temperature both the γ and γ' phases of a particular composition have identical free energy) for the alloy composition. Thermodynamic calculations showed that the T_0 temperature for Ni–12.1 at.% Al–9.05% Co–9.12% Cr system is 1009 K (736°C). Surprisingly, the calculated diffusion controlled growth rates drop rapidly near to this temperature (see Fig. 12). Therefore, if the Ni–Al–Co–Cr alloy can be undercooled to such a low temperature by rapid cooling, the congruent ordering and phase separation can be initiated. However, if the undercooling is not so severe, nucleation and growth will be the governing mechanisms.

This transformation sequence might have occurred in the water-quenched samples, provided that such undercooling was achieved. It is important to note that congruent ordering necessitates only short-range diffusion. However, phase separation necessitates long range diffusion. The observed local compositional changes could be associated with this incomplete phase separation event. As the above theory allows for homogeneous ordering and subsequent phase separation, it does allow the precipitates to be interconnected in space. It is important to note that the schematic diagram shown in Fig. 13 is for a binary alloy system and thermodynamic free energy variation in a multicomponent system is expected to be much more complex.

The consequence of the observed microstructural development is significant. Previous researchers have shown that the microstructure of nickel base superalloy controls the final high-temperature properties [8, 9]. The nonequilibrium composition of phases will also control the lattice misfit between the γ and γ' phases [2, 3] which, in turn, will control the tendency for the formation of rafts during high-temperature service [29]. Therefore, the results are relevant to the high-temperature performance of welded SX and DS nickel base superalloys used in the as-welded conditions without any homogenization and heat-treatments. Further work is necessary to understand the stability of these microstructures under controlled high temperature thermal cycles.

5. CONCLUSIONS

The precipitation of $L1_2$-ordered γ' precipitates from the γ phase was investigated under continuous cooling conditions that may be experienced in a typical welding process. The dilatation characteristics were measured during such conditions and show distinctions between samples cooled at different rates. The number density of γ' precipitates increased, then size decreased, and the morphology changed from cuboidal to irregular shape as the cooling rate increased. Under slow cooling conditions of 1 K s^{-1}, small (~20 nm) secondary γ' precipitates were observed, in addition to the coarse primary γ' precipitates. Under rapid water-quenched conditions, the γ' precipitate size (~50 nm) reduced significantly and their morphologies were complex.

Atom probe analyses of water-quenched sample indicated an interconnected γ' phase morphology, nonequilibrium partitioning of alloying elements between the γ and γ' phases, i.e., Co-enriched regions within the γ' phase and Al-enriched regions within the γ phase. The measured composition of γ phase from this sample was different compared to slow cooled samples. The compositional variation of the primary γ' precipitates from samples subjected to different cooling rate was small. The secondary γ' precipitates that formed during slow cooling at 1 K s^{-1} had slightly lower Al concentration than those of the primary γ' precipitate.

The observed increase in the number density of the γ' precipitates with cooling rate was attributed to an increase in driving force for the precipitation of the γ' phase from the γ phase and through nucleation and growth calculations. However, the rapid increase in number density, localized enrichment of Co and the complex morphology of the γ' phase observed in water-quenched samples is attributed to a congruent ordering and phase separation mechanism.

Acknowledgements—This research at Oak Ridge National Laboratory (ORNL) and SHaRE user facility was sponsored by the Division of Materials Science and Engineering, US Department of Energy, under contract DE-ACO5-00OR22725 with UT-Battelle, and through the SHaRE Program under contract DE-AC05-76OR00033 with Oak Ridge Associated Universities. The authors thank Drs. E. Kenik and S. Agnew of Oak Ridge National Laboratory for helpful discussions. The authors also thank R. W. Reed, K. F. Russell and W. Jones of ORNL for help in specimen preparations. We acknowledge the support of SIEMENS-Westinghouse for providing materials used in this investigation.

REFERENCES

1. David, S. A. *et al.*, *Science and Technology of Welding and Joining*, 1997, **2**, 79.
2. Babu, S. S., David, S. A. and Miller, M. K., *Appl. Surf. Sci.*, 1996, **94-95**, 280.
3. Babu, S. S. *et al.*, *J. Phys. IV*, 1996, **6**, C5.
4. Ardell, A. J., Nicholson, R. B. and Eshelby, J. D., *Acta metall.*, 1966, **14**, 1295.
5. Ardell, A. J., *Acta metall.*, 1968, **16**, 511.
6. Wendt, H. and Haasen, P., *Acta metall.*, 1983, **31**, 1649.
7. Blavette, D., Buchon, A. and Chamberland, S., in *Proc. Euromat Conference, Aachen*, ed. H. E. Exner and V. Schumacher. Dgm Information Gesellschaft Verlag, Germany, 1989, p. 419.
8. MacKay, R. A. and Nathal, M. V., in *MICON86: Optimization of Processing, Properties, and Service Performance Through Microstructure Control*, ed. B. L. Bramfit, R. C. Benn, C. R. Brinkman and G. F. Vander Voort., ASTM STP 979. American Society for Testing and Materials, Philadelphia, PA, 1988, p. 202.
9. MacKay, R. A. and Ebert, L. J., in *Proc. 5th International Conference on Superalloys*, ed. M. Gell. AIME, New York, 1984, p. 135.
10. Blavette, D., Cadel, E. and Deconihout, B., *Mater. Characterization*, 2000, **44**, 133.
11. Schmuck, C., Caron, P., Hauer, A. and Blavette, D., *Phil. Mag. A*, 1997, **76**, 527.
12. Jackson, M. P., Starnik, M. J. and Reed, R. C., *Mater. Sci. Eng. A*, 1999, **A264**, 26.
13. Wood, J. V., Mills, P. F., Bingham, J. K. and Bee, J. V., *Metall. Trans. A.*, 1979, **10A**, 575.
14. Touloukian, Y. S., Kirby, R. K., Taylor, R. E. and Desai, P. D., in *Thermophysical Properties of Matter*, Vol. 12. IFI/Plenum, New York, 1975.
15. Miller, M. K., *J. Phys.*, 1986, **47**, 493.
16. Miller, M. K., *J. Micros.*, 1997, **186**, 1.
17. Hyde, J. M. *et al.*, *Surf. Sci.*, 1992, **266**, 370.
18. Thermal Expansion of Alloys Used in Power Generation, EPRI RD-3685, Final Report. Electric Power Research Institute, September 1984.
19. Sundman, B., Jansson, B. and Andersson, J. O., *Calphad*, 1985, **9**, 1.
20. Saunders, N., *Ni-Data Information*. Thermotech Ltd., Surrey Technology Center, Guidford, Surrey GU2 5YG, UK, 1998.
21. Cahn, R. W. and Haasen, P. (ed.), *Physical Metallurgy, Part I*. Elsevier, Amsterdam, 1983, p. 415.
22. Engström, A., Höglund, L. and Ågren, J., *Metall. Mater. Trans. A.*, 1994, **25A**, 1127.
23. Wang, D. -Q., Babu, S. S., Payzant, E. A., Radaelli, P. G. and Hannon, A. C., *Metall. Mater. Trans. A.*, 2001, **32A**, 1551.
24. Wang, Y., Banerjee, D., Su, C. C. and Khachaturyan, A. G., *Acta mater.*, 1998, **46**, 2983.
25. Simmons, J. P., *Ordering and Phase Separations in FCC/$L1_2$ Alloys*. PhD thesis, Carnegie Mellon University, 1992.
26. Soffa, W. A. and Laughlin, D. E., *Acta metall.*, 1989, **37**, 3019.
27. Khachaturyan, A. G., Lindsey, T. F. and Morris, J. W., *Metall. Trans. A*, 1988, **19A**, 249.
28. Sigli, C. and Sanchez, J. M., *Acta metall.*, 1985, **33**, 1097.
29. Saito, M., Aoyama, T., Hidaka, K., Tamaki, H., Ohashi, T., Nakamura, S. and Suzuki, T., *Scripta mater.*, 1996, **34**, 1189.